catalysts

MDPI

Article

Bifunctional Co_3O_4/ZSM-5 Mesoporous Catalysts for Biodiesel Production via Esterification of Unsaturated Omega-9 Oleic Acid

Francisco Núñez [1], Lifang Chen [1,*], Jin An Wang [1], Sergio Ordin Flores [1], José Salmones [1], Ulises Arellano [2,3], Luis Enrique Noreña [4,*] and Francisco Tzompantzi [3]

[1] Escuela Superior de Ingeniería Química e Industrias Extractivas, Instituto Politécnico Nacional, Col. Zacatenco, Ciudad de México 07738, Mexico
[2] Colegio de Ciencias y Humanidades, Universidad Autónoma de la Ciudad de México, Ciudad de México 09620, Mexico
[3] Departamento de Química, Universidad Autónoma Metropolitana-Iztapalapa, Av. San Rafael Atlixco No. 186, Ciudad de México 09340, Mexico
[4] Departamento de Ciencias Básicas, Universidad Autónoma Metropolitana-Azcapotzalco, Av. San Pablo 180, Col. Reynosa Tamaulipas, Ciudad de México 02200, Mexico
* Correspondence: lchen@ipn.mx (L.C.); lnf@azc.uam.mx (L.E.N.)

Abstract: In the present work, two sets of the Co/ZSM-5 mesoporous catalysts with different acidity and Co loadings varying from 1 to 5 and 10 wt% were prepared using mesoporous ZSM-5-A (Si/Al = 50) and ZSM-5-B (Si/Al = 150) as support. X-ray diffraction (XRD) analysis showed that the Co_3O_4 phase was formed in the surface of catalysts and the reducibility of Co_3O_4 nanoparticles on the ZSM-5-B was greater in comparison with that on the ZSM-5-A solid. In situ FTIR of pyridine adsorption characterization confirmed that all of the Co/ZSM-5 catalysts contained both Lewis (L) and Brønsted (B) acid sites, with a relatively balanced B/L ratio ranging from 0.61 to 1.94. Therefore, the Si/Al molar ratio in ZSM-5 affected both the surface acidity and the cobalt oxide reducibility. In the esterification of unsaturated omega-9 oleic acid with methanol, under the optimal reaction conditions (temperature 160 °C, catalyst concentration 2 g/L, methanol/oleic acid molar ratio 30, and reaction time 180 min), the biodiesel selectivity reached 95.1% over the most active 10 wt% Co/ZSM-5-B catalyst. The higher esterification activity of the Co/ZSM-5-B catalysts can be correlated with the greater amount of B and L acid sites, the balanced B/L ratio, and the higher reducibility of Co_3O_4 nanoparticles. The oleic acid esterification reaction followed the bifunctional mechanism of combining metal function (dispersed Co_3O_4 with a greater reducibility) with the acidity function (both B and L acid sites with a relative balanced B/L ratio) on the catalysts, which may help in providing a deep understanding of the esterification pathways and benefiting the design of novel bifunctional catalysts for biofuel production.

Keywords: esterification; oleic acid; Co/ZSM-5; bifunctional mechanism; biodiesel

check for updates

Citation: Núñez, F.; Chen, L.; Wang, J.A.; Flores, S.O.; Salmones, J.; Arellano, U.; Noreña, L.E.; Tzompantzi, F. Bifunctional Co_3O_4/ZSM-5 Mesoporous Catalysts for Biodiesel Production via Esterification of Unsaturated Omega-9 Oleic Acid. *Catalysts* **2022**, *12*, 900. https://doi.org/10.3390/catal12080900

Academic Editors: Diego Luna and Valeria La Parola

Received: 6 June 2022
Accepted: 10 August 2022
Published: 16 August 2022

1. Introduction

Biodiesel is an alternative to fossil petroleum and can be produced from renewable resources, such as palm oil, canola oil, soya bean oil, and rape seed oil [1,2]. Compared to fossil diesel, biodiesel can reduce the generation of particulates with a low concentration of carbon monoxide in the emissions. More importantly, almost no sulfur oxides are released in the combustion exhaust of biodiesel. Natural or synthetic biodiesel has other advantages over mineral, oils such as higher biodegradability and high flash points [3]. Esterification and transesterification reactions are widely applied in biodiesel production via catalytic techniques [4,5]. The conventional biodiesel production process utilizes homogeneous basic catalysts, such as liquid NaOH and KOH, and acidic catalysts, such as H_2SO_4, which merge as part of the products at the end of the processes. In order to comply with increasingly strict environmental regulations, the salts and by-product glycerol in biodiesel mixtures must be neutralized and removed. The soap that is formed in the mixture shows surfactant characters that allow them to strongly adhere to the methyl ester fractions during liquid–liquid separation [3,4]. Moreover, the extra homogeneous catalysts cannot be recovered after the reactions. All of these drawbacks reduce the environmental acceptability of the homogeneous acidic or basic catalysis processes. Currently, more attention is focused on recyclable and reusable heterogeneous catalysts for biofuel production [6–8].

The ideal characteristics of heterogeneous catalysts for biofuel production are high catalytic activity and stability, minimal lixiviation, and low cost. Hence, the selection of an appropriate solid catalyst and reaction feedstock, and the optimization of reaction conditions, are foremost in large-scale biodiesel production. Heterogeneous base and acid catalysts have been intensely investigated. Base catalysts, such as alkaline earth oxides (including magnesium oxide (MgO), calcium oxide (CaO), and strontium oxide (SrO)), mixed metal oxides, hydrotalcites, anionic resins, and others, have been used in biodiesel production [9–13]. These base catalysts have advantages over solid acid catalysts because they can catalyze reactions at lower reaction temperature with higher catalytic activity. However, the utilization of base catalysts is limited to refined vegetable oils containing less than 0.5 wt% free fatty acids (FFAs). Under basic conditions, excess soap may be produced due to the hydroxylation of high FFA content, which leads to increases in purification costs when oils with high FFA content are used as feedstock. The use of heterogeneous acid catalysts can effectively avoid these negative influences.

Heterogeneous acid catalysts can simultaneously drive FFA esterification reactions and tolerate the water content in the feedstocks [14]. However, acid catalysts require severe reaction conditions to effectively transform oil into biodiesel; thus, acid catalysts must have sufficient thermal stability. Although acid catalysts have attracted less attention than the basic counterparts due to their low reaction rates, a variety of acidic solid materials have been tested for biodiesel production [15,16]. For example, the Zr-SBA-15/bentonite catalyst was reported to be very active in biodiesel production, showing a fatty acid methyl ester (FAME) yield of approximately 96% at 210 °C and 70 bar in a continuous reactor, with a methanol to oil molar ratio of 50 and a residence time of 30 min [17]. Although the application of acid catalysts results in harsher reaction conditions than does the application of base catalysts, acid catalysts are still attractive because they use less expensive low-quality feedstock.

Heterogeneous acid catalysts, such as Pd/C [18], Pt/C [19], Pt/Al_2O_3 [20], Pd/$BaSO_4$ [21,22], Pd/SBA-15 [23], TiO_2/SiO_2 [24,25], $SnCl_2 \cdot 2H_2O$ [26], and Na_2MoO_4 [27], were reported as active in biofuel production, allowing them to be separated for reuse by filtration of the reaction mixture. The esterification of fatty acids was investigated using SO_4/ZrO_2, heteropolyacids of tungsten and molybdenum, andCs-exchanged heteropolyacids [28,29]. Transition metal oxides, such as Fe, Co, Ni, and Cu oxides, when supported by zeolites, alumina, or ZrO_2, exhibited good catalytic activity [4,7].

ZSM-5 microzeolites have large surface areas with high thermal stability and stable acidity. They have been used as catalyst supports for many acidic catalytic reactions, including biofuel production [30–32]. However, due to some limitations of the micropores in ZSM-5, light olefins are often formed in the esterification and transesterification of long chain fatty acids by cracking. Therefore, the use of mesoporous zeolites as catalysts is more interesting in biodiesel production.

In previous research, the influence of Brønsted (B) acidity on esterification was intensely investigated. In fact, zeolite contained both Lewis and Brønsted acid sites. However, the role of Lewis (L) acidity in biofuel production was not thoroughly investigated. The influence of Lewis and Brønsted acid sites and the B/L ratio in zeolites on catalytic activity is an attractive topic for investigation.

The main focus of the present work is the use of mesoporous ZSM-5 as the parent material and cobalt oxide as the dopant to obtain Co/ZSM-5 mesoporous catalysts for biodiesel production via the esterification of unsaturated omega-9 oleic acid as feedstock. Oleic acid is abundant in the southern region of Mexico and can be obtained from vegetable oils, canola oil, safflower oil, olive oil, mustard oil, and nut oils. Cobalt oxide was used as the dopant of zeolite to modify the acidity and catalytic activity. As hydrophobic and hydrophilic characteristics, as well as the acidity of zeolites, are related to the Si/Al ratio, two mesoporous zeolites, with low and high Si/Al ratios (50 and 150), were investigated. Two series of mesoporous Co/ZSM-5 catalysts were synthesized by the impregnation method, and the effects of the Si/Al atomic ratio in ZSM-5 on catalytic activity were investigated. We found that surface acidity, together with a balanced B/L ratio and the reducibility of the dispersed cobalt oxides, played crucial roles in oleic acid esterification with methanol. A bifunctional reaction mechanism of combining the surface acidity function with the metal function was proposed. This study may help in providing a deep understanding of the esterification pathways and benefiting the design of novel catalysts for biofuel production.

2. Results and Discussion

2.1. Textural Properties: Nitrogen Physisorption Analysis

Figure 1 shows the hysteresis loops of N_2 adsorption-desorption isotherms of the Co/ZSM-5-A and Co/ZSM-5-B catalysts. These loops showed isotherm profiles type IV, according to the classification of the International Union of Pure and Applied Chemistry (IUPAC) [33], which possess the characteristics of mesoporous materials. The main textural parameters are reported in Table 1. The pure ZSM-5-A and ZSM-5-B solids had surface areas of 408 m^2g^{-1} and 398 m^2g^{-1} with pore diameters of 86 Å and 75 Å, respectively. These solids differ from the normal microporous ZSM-5 zeolites, which usually have average pore diameters of approximately 5–7 Å. The mean pore diameter of our mesoporous zeolites was 10 times greater than that of traditional ZSM-5 solids. The micropore volume was lower than 0.055 cm^3/g, which is much smaller than the total pore volume (0.76 cm^3/g for ZSM-5-A and 0.83 cm^3/g for ZSM-5-B). The loops of the N_2 adsorption–desorption isotherms of ZSM-5-A and ZSM-5-B are presented in Figures S1 and S2 in the Supplementary Materials. The Co-loaded catalysts had smaller surface areas than those with bare ZSM-5 support. The surface areas diminished as the cobalt contents increased, due to the partial blockage of some zeolite pores by cobalt moieties.

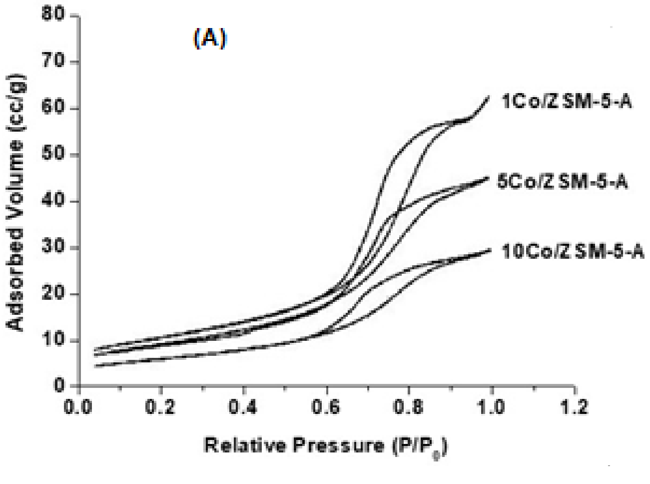

Figure 1. *Cont.*

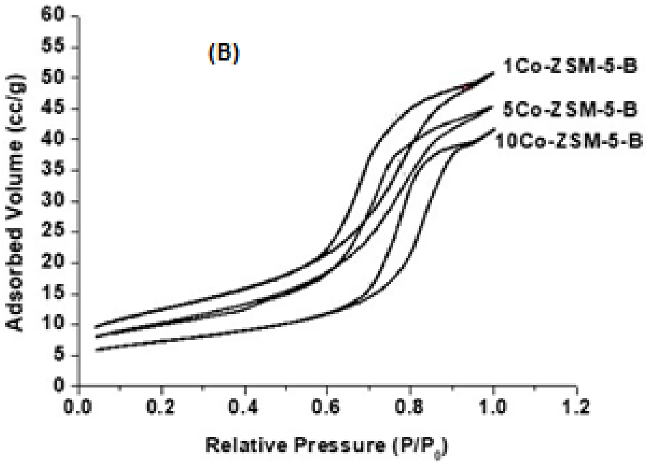

Figure 1. Loops of N_2 adsorption–desorption isotherms of catalysts. (**A**): Co/ZSM-5-A (Co content varying from 1 wt% to 10 wt%); (**B**): Co/ZSM-5-B (Co content varying from 1 wt% to 10 wt%).

Table 1. Textural properties of ZSM-5-A-, ZSM-5-B-, and Co-supported catalysts.

Catalyst	BET Area (m^2/g)	Average Pore Diameter (Å)
ZSM-5-A	408	86
ZSM-5-B	398	75
1Co/ZSM-5-A	402	81
5Co/ZSM-5-A	382	67
10Co/ZSM-5-A	346	59
1Co/ZSM-5-B	366	69
5Co/ZSM-5-B	353	60
10Co/ZSM-5-B	321	47

2.2. Co Content and Si/Al Molar Ratio Determination: Atomic Absorption Spectroscopy (AAS)

The actual cobalt contents in the Co/ZSM-5 catalysts and the Si/Al molar ratio in the ZSM-5 and Co/ZSM-5 catalysts obtained by atomic absorption spectroscopic analysis are reported in Table 2. The Co content in the Co/ZSM-5-A and Co/ZSM-5-B catalysts were very close to their nominal values. However, the Si/Al molar ratio varied after Co impregnation. For the ZSM-5-A sample, the real Si/Al ratio was 49.3; it increased in the Co/ZSM-5-A catalysts. However, the Si/Al ratio in the Co/ZSM-5-B catalysts remained stable, close to the value of the parent zeolite. The Si/Al molar ratio changes indicated that dealuminum took place during the cobalt nitrate impregnation procedure. The high aluminum content in the ZSM-5-A sample led to more extra-framework aluminum removal from zeolite in the catalyst preparation.

Table 2. Co content and Si/Al ratio in ZSM-5 supports and Co/ZSM-5-A and Co/ZSM-5-B catalysts.

Catalysts	Real Co Content (wt%)	Nominal Co Content (wt%)	Si/Al Molar Ratio
ZSM-5-A			49.3
ZSM-5-B			148.6
1Co/ZSM-5-A	1.04	1	70.6
5Co/ZSM-5-A	4.80	5	62.1
10Co/ZSM-5-A	9.89	10	64.6
1Co/ZSM-5-B	0.96	1	145.7
5Co/ZSM-5-B	4.86	5	146.4
10Co/ZSM-5-B	9.89	10	148.2

2.3. Crystalline Structure: X-ray Diffraction Analysis

Figure 2 shows the XRD patterns of the pure ZSM-5-A and ZSM-5-B solids. The ZSM-5 zeolites have intense diffraction peaks and well-defined XRD patterns, especially those zeolites that are located at 2θ of 7~9° and 23–25°, indicating high crystallinity (JCPDS card number 00-044-0002).

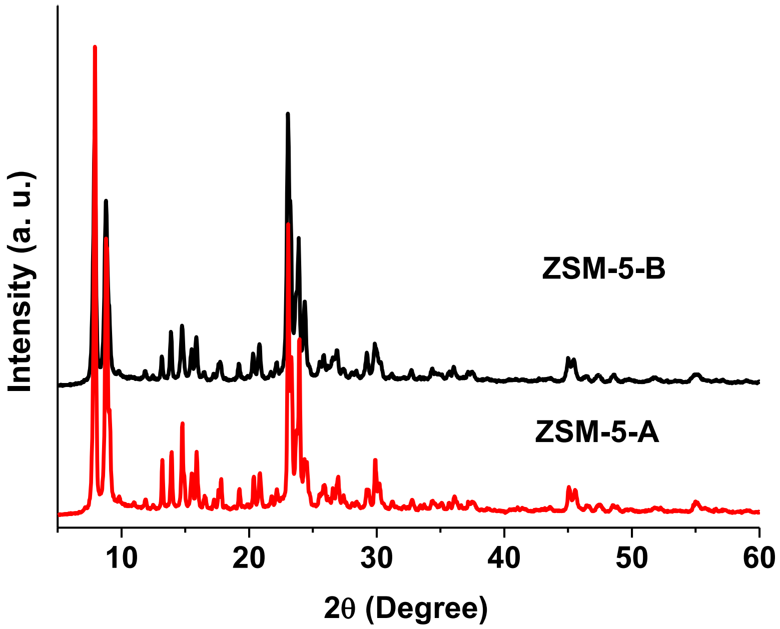

Figure 2. X-ray diffraction patterns of the ZSM-5 zeolite.

For Co/ZSM-5 fresh catalysts dried at 120 °C, as shown in Figure 3, the characteristic XRD patterns of the ZSM-5 zeolites confirmed that the zeolite structures were well maintained. There was a sharp peak at 18.8°, corresponding to the reflection of the (001) plane of $Co(NO_3)_2$ crystals [34], and a weak peak at 41.3°, corresponding to the (200) plane of the fcc-type CoO (JCPDS 05-0727). For the sample 1Co/ZSM-5, CoO domains with small size should develop, as no obvious characteristic reflection of cobalt oxide was observed in the XRD patterns. For the samples with 5 wt% and 10 wt% of Co, the Co/ZSM-5 catalysts exhibited an increased intensity of the CoO peak at 41.3° [35], while the intensity of the peaks related to the ZSM-5 solids decreased when cobalt loading increased, due to the effects of deposition and the coverage of Co oxides. A larger crystallite size was observed on the samples with 5 wt% and 10 wt% Co content.

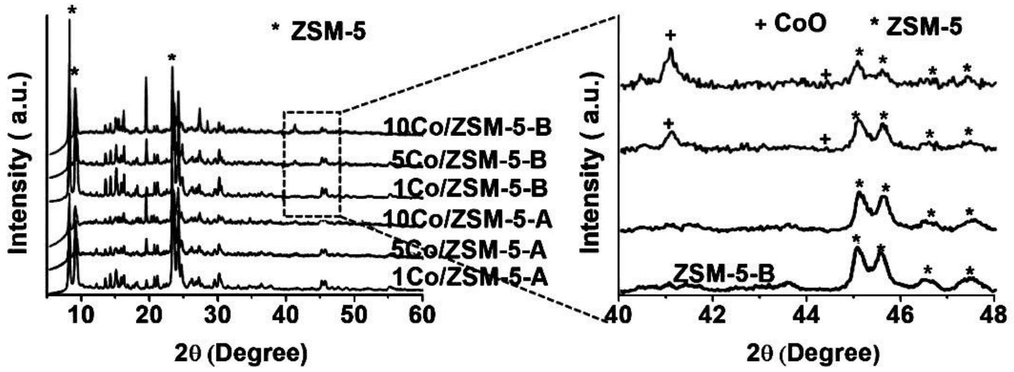

Figure 3. X-ray diffraction patterns for fresh Co/ZSM-5-A and Co/ZSM-5-B catalysts.

When the Co/ZSM-5 catalysts were calcined at 500 °C, the sharp peak at 18.8° disappeared, indicating the thermal decomposition of $Co(NO_3)_2$ crystals. Accordingly, several peaks at 2θ of 31.7, 37.2, 59.4, 59.7°, and 66.2° appeared, which were attributed to the reflections of the (220), (311), (511), and (440) planes of the Co_3O_4 crystalline structure dispersed on the zeolite (Figure 4). During calcination in air, the $Co(NO_3)_2$ was decomposed into CoO, which reacted with O_2 in air to produce Co_3O_4 crystals [36].

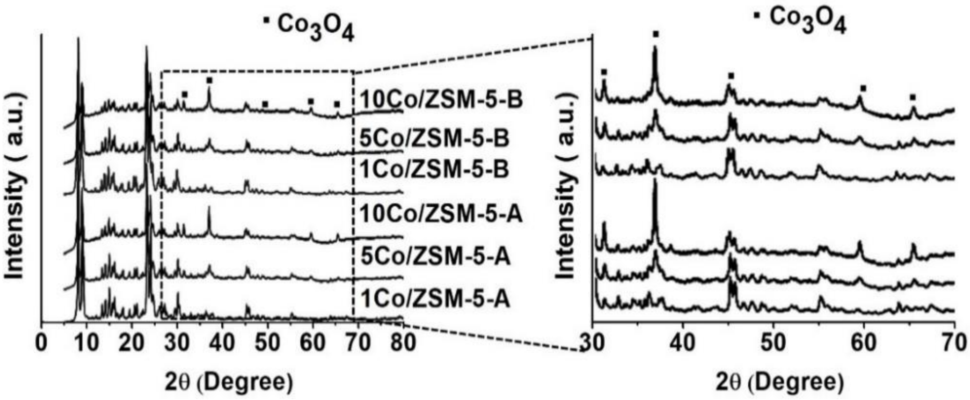

Figure 4. XRD patterns of the Co/ZSM-5-A and Co/ZSM-5-B catalysts calcined at 500 °C.

Based on the XRD results shown in Figure 4, it was possible to conclude that calcination led to the oxidation of some Co^{2+} to Co^{3+}, forming larger crystals of cobalt oxide (Co_3O_4), consisting of equivalent molar CoO and Co_2O_3 phases. The average Co_3O_4 crystallite size obtained using Scherrer's formula was approximately 22 nm to 26 nm, depending on the Co content.

For the 1Co/ZSM-5-A and 1Co/ZSM-5-B catalysts, only the typical pattern of ZSM-5 peaks was shown and no Co_3O_4 characteristic peaks were observed. These observations indicated that Co_3O_4 were homogeneously dispersed on the ZSM support with very small particle sizes (<4 nm). The peak intensity of the peaks corresponding to the Co oxides increased as the Co content increased to 5 wt% and 10 wt%, indicating crystallite size growth with higher Co content. However, the intensity of the XRD peaks of the 10Co/ZSM-5-A sample was higher than that of 10Co/ZSM-5-B, suggesting that higher dispersion of Co_3O_4 was achieved on ZSM-5-B zeolites. Therefore, support with a higher Si/Al molar ratio favored the formation of highly dispersed cobalt oxides.

2.4. Surface Species: Raman Spectroscopy

Figure 5 shows the Raman spectra of the ZSM-5-A and ZSM-5-B zeolites. The bands between 850 cm^{-1} and 190 cm^{-1} with low intensity indicate the siloxane bridges of the zeolite structure [36]. For the 1Co/ZSM-5-A and 1Co/ZSM-5-B catalysts, the Raman features shown in Figure 6 were rather similar to those of bare zeolite, where the broad band located at approximately 362 cm^{-1} was attributed to the structure of the ZSM-5 zeolite. For the Co/ZSM-5-A and Co/ZSM-5-B catalysts with 5 wt% and 10 wt% Co (Figure 6), the Raman spectra related to the Co_3O_4 crystals showed four Raman-active modes in the range of 400 nm to 800 nm. They were located at approximately 687, 615, 518, and 480 cm^{-1}, corresponding to the A_{1g}, $F_{2g\,(2)}$, and E_g modes of the cobalt oxide (Co_3O_4) spinel microcrystals [37]. The strong band at 689 cm^{-1} was assigned to Raman vibration of Co^{3+}–O^{2-}; which is characteristic of octahedral sites ($Co^{III}O_6$) and belongs to the A_{1g} species in the O_h spectroscopic symmetry. The weak band located at 615 cm^{-1} had $F_{2g\,(1)}$ symmetry [38,39]. The increased band intensity with Co content was indicative of a rearrangement from dispersed CoO to Co_3O_4 crystals, which is in good agreement with the XRD analysis shown in Figure 4.

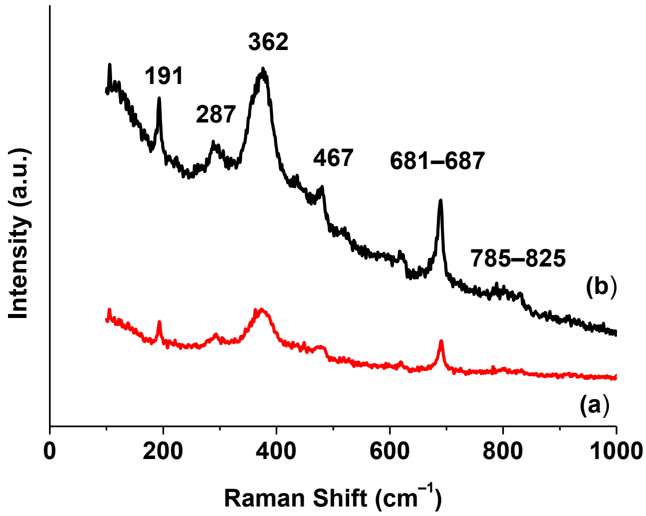

Figure 5. Raman spectra of ZSM-5-A (**a**) and ZSM-5-B (**b**).

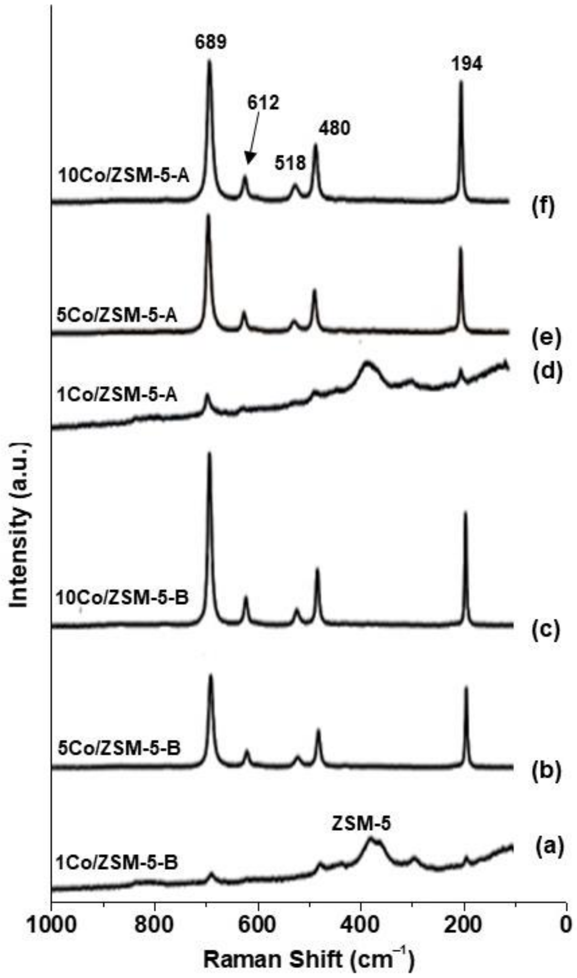

Figure 6. Raman spectra of the Co/ZSM-5 catalysts: (**a**) 1Co/ZSM-5-A, (**b**) 5Co/ZSM-5-A, (**c**) 10Co/ZSM-5-A, (**d**) 1Co/ZSM-5-B, (**e**) 5Co/ZSM-5-B, (**f**) 10Co/ZSM-5-B.

2.5. Surface Acidity: In Situ FTIR Spectroscopy of Pyridine Adsorption (FTIR-Py)

Figure 7 shows the in situ FTIR spectra of pyridine adsorption on the ZSM-5-A and ZSM-5-B supports, recorded at 150 °C. Both the ZSM-5-A and ZSM-5-B supports presented the Lewis (L) and Brønsted (B) acid sites. The band at 1445 cm^{-1} was attributed to pyridine adsorption on the Lewis acid sites and the band at approximately 1540 cm^{-1} indicated pyridine adsorption on the Brønsted acid sites. The band at 1490 cm^{-1} resulted from pyridine molecule association with both the Lewis and Brønsted acid sites as neighbors [40–42]. It is noted that the ZSM-5-A presented a similar amount of Brønsted acidity as the ZSM-5-B; but a greater number of Lewis acid sites were formed. This resulted from the higher concentration of aluminum in zeolite-A sample (Si/Al = 50), where more extra-framework Al^{3+} existed in ZSM-5-A, leading to more L acid sites in the zeolite [43].

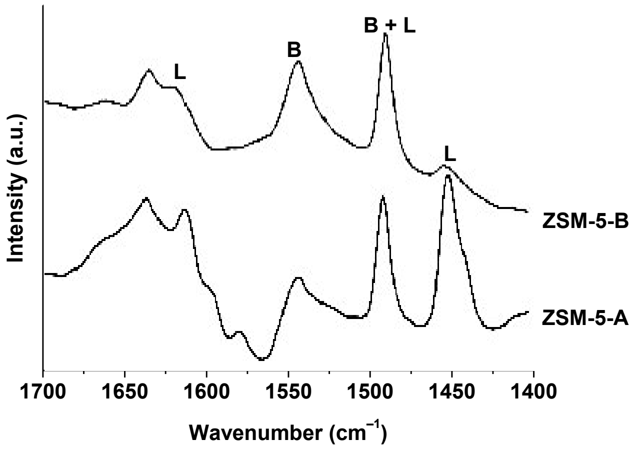

Figure 7. In situ IR spectra of pyridine on ZSM-5-A and ZSM-5-B. L: Lewis acidity; B: Brønsted acidity.

For all of the Co/ZSM-5 catalysts, the in situ FTIR-Py spectra (Figure 8) showed strong bands at 1445, 1490, and 1540 cm^{-1}, indicating that pyridine coordinated on L, B, or both B and L acid sites. Usually, the physisorption of pyridine on zeolite-related materials occurs at temperatures below 150 °C; therefore, the chemisorbed pyridine can be recorded at 150 °C or above. The number of acid sites increased with increases of Co content for both series of catalysts. With respect to the Lewis acidity in the parent ZSM-5-A, the Lewis acidity in Co/ZSM-5-A catalysts significantly reduced. This resulted from the dealuminum phenomenon in the catalysts during Co impregnation. More extra-framework removal led to a decrease in Lewis acidity.

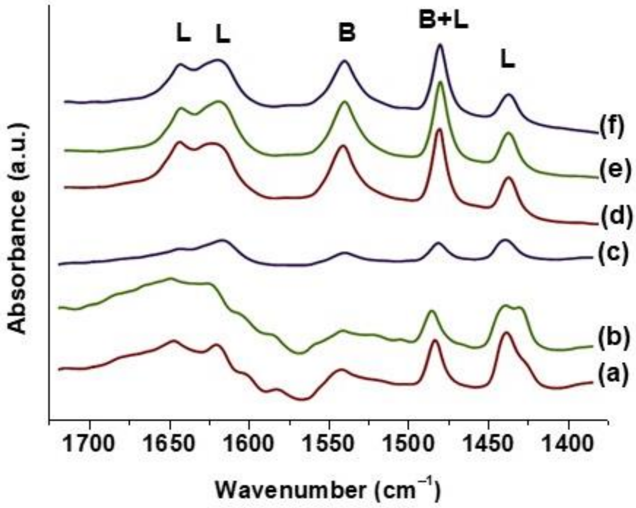

Figure 8. IR spectra of pyridine on the Co/ZSM-5 catalysts recorded at 150 °C. (**a**) 10Co/ZSM-5-A; (**b**) 5Co/ZSM-5-A; (**c**) 1Co/ZSM-5-A; (**d**) 10Co/ZSM-5-B; (**e**) 5Co/ZSM-5-B; (**f**) 1Co/ZSM-5-B. L: Lewis acidity; B: Brønsted acidity.

Figure 9 shows the total acidity of the catalysts Co/ZSM-5-A and Co/ZSM-5-B obtained at different temperature. For the Co/ZSM-5-B catalysts, the acid data did not significantly vary with temperatures between 100 °C and 300 °C, indicating stable acid strength. The variation of acidity on the Co/ZSM-5-B catalysts decreased at higher temperatures. The immobilization of cobalt oxide onto ZSM-5 led to an increment in total acidity because of the acidic character of Co_3O_4. The amount of total acidity increased as the Co content increased. The number of total acid sites that were present on the Co/ZSM-5-B catalysts increased by 5% to 8% in comparison with the total acid sites that were present on the Co/ZSM-5-A catalysts.

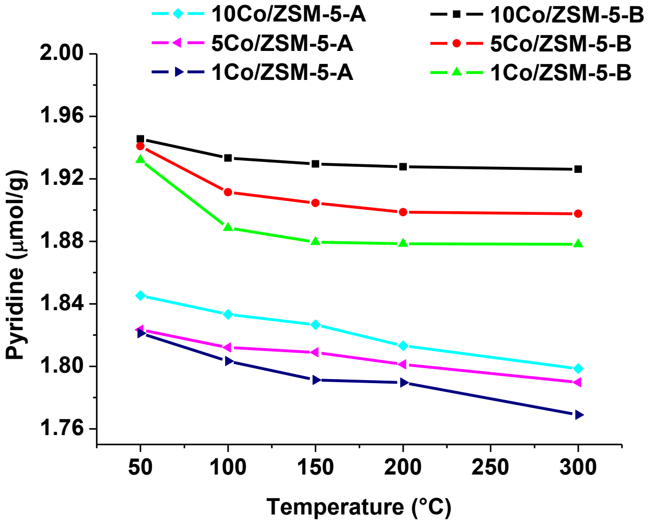

Figure 9. Pyridine adsorbed on B acid sites as a function of the desorption temperature.

2.6. Reducability: TPR-H_2

Figure 10 shows the TPR-H_2 profiles of the two 10Co/ZSM-5 samples. Two peaks were observed in the temperature range between 127 °C and 427 °C and between 527 °C and 727 °C, respectively. The two H_2-TPR peaks may indicate the reduction of Co_3O_4 to CoO and CoO to Co, respectively [44,45]. The area of the high temperature reduction peak was almost twice the area of the low temperature reduction peak, which can be explained by Equations (1) and (2) during the reduction procedure:

$$Co_3O_4 + H_2 \rightarrow 3CoO + H_2O \quad (1)$$

$$3CoO + 3H_2 \rightarrow 3Co + 3H_2O \quad (2)$$

The area of the TPR-H_2 peak formed at 10Co/ZSM-5-B was much greater than that on the 10Co/ZSM-5-A, indicating that the amount of the reducible Co_3O_4 and CoO phases on the surface of 10Co/ZSM-5-B were much greater. The difference in the reducibility of the cobalt oxides seemed to be related to the aluminum content in the zeolite. The ZSM-5-A had a Si/Al molar ratio of 50; after 500 °C calcination, some extra-framework alumina in the Co/ZSM-5-A sample probably reacted with cobalt oxide to form $CoAl_2O_4$, which has rather low reducibility and is usually inactive for esterification reaction. However, based on the XRD patterns shown in Figure 4, the formation of the $CoAl_2O_4$ spinel phase was not detectable, probably because of the small amount and small crystallite size of the $CoAl_2O_4$ spinel.

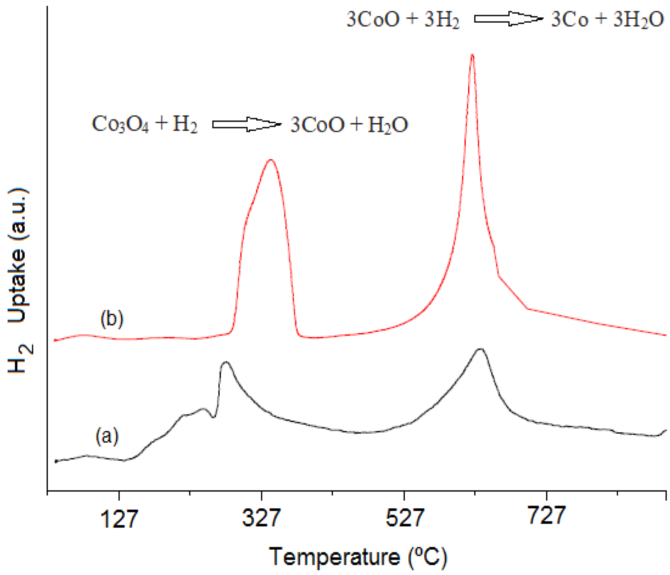

Figure 10. H_2-TPR profiles of the catalysts. (**a**) 10Co/ZSM-5-A; (**b**) 10Co/ZSM-5-B.

2.7. Morphological Feature

The transmission electron microscopy (TEM) technique was used to observe the particle size distribution of the cobalt oxide nanoparticles and the morphological feature of the Co/ZSM-5-A and Co/ZSM-5-B catalysts. Many small crystals are homogeneously distributed on the surface of ZSM-5 solids. To determine the average population and particle size for each catalyst, the following equation was used: $d_s = \Sigma n_i d_i^3/\Sigma n_i d_i^2$, where d_s is the average particle size, di is the particle diameter, and n_i is the number of particles with diameter d_i. These crystals had sizes of approximately 3 nm to 5 nm for the 5Co/ZSM-5-A (Figure 11a) and 5Co/ZSM-5-B (Figure 11b) catalysts. They must belong to cobalt oxides in combination with the analysis of the TEM observation with the results of XRD. The Co_3O_4 particle distribution on the 10Co/ZSM-5-A and 10Co/ZSM-5-B catalysts was not very homogeneous, and the average particle size was around 10 nm to 25 nm (Figure 11c,d) for both the 10Co/ZSM-5-A and 10Co/ZSM-5-B catalysts.

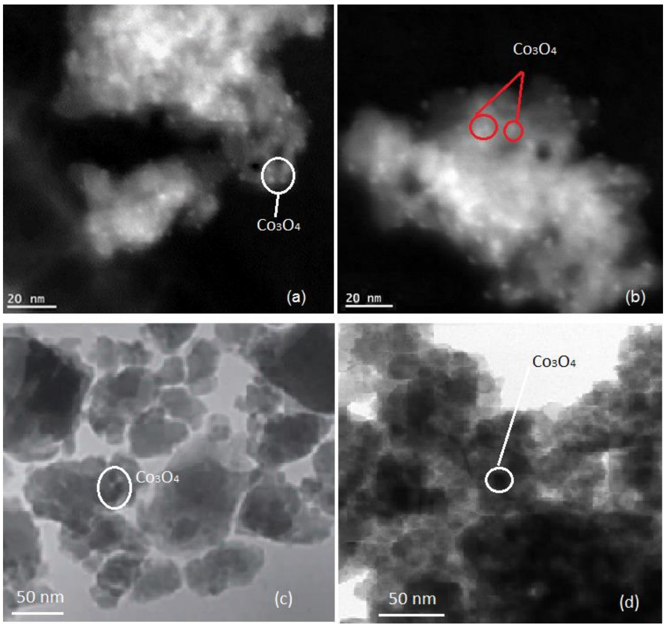

Figure 11. TEM images of the Co/ZSM-5 catalysts. (**a**) 5Co/ZSM-5-A; (**b**) 5Co/ZSM-5-B; (**c**) 10Co/ZSM-5-A; (**d**) 10Co/ZSM-5-B.

2.8. Catalytic Evaluation and Biodiesel Production

2.8.1. Oleic Acid Conversion and Biodiesel Yield

In the esterification of oleic acid with methanol, in order to overcome the equilibrium limitation, the molar ratio of methanol to oleic acid was set at 30. Therefore, the esterification reaction was performed under an alcohol excess condition. To determine the effect of the reaction temperature on the oleic acid conversion, the reaction temperature varied between 140 °C and 170 °C, according to our experimental experience and the literature [46,47]. Figure 12 shows the oleic acid C/C_0 values as a function of reaction time (total 180 min) obtained at different temperatures using 5 wt% Co/ZSM-5-B catalyst. The oleic acid concentration decreased with an increase in reaction time. After 130 min of reaction, the C/C_0 values were almost stable. Oleic acid conversion increased as the temperature increased from 140 °C to 150 °C and 160 °C. The catalytic activity was not obviously increased at 170 °C compared with the activity obtained at 150 °C. Therefore, in the following reaction, the reaction temperature was set at 160 °C.

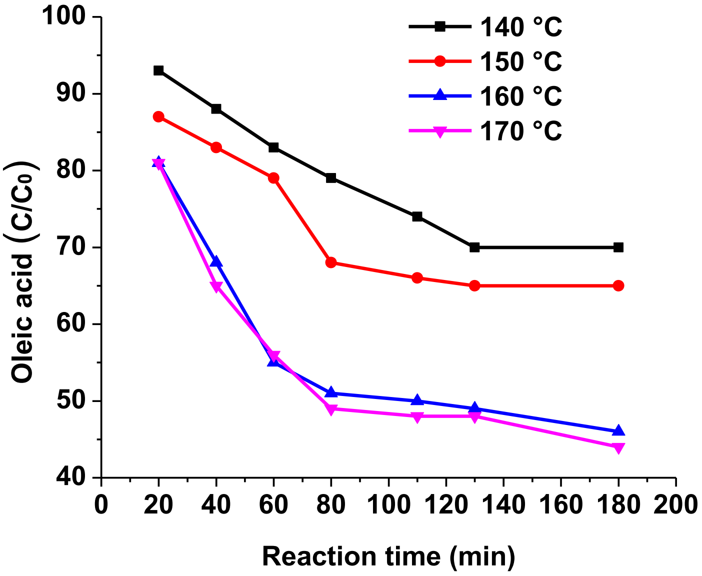

Figure 12. Oleic acid (C/C_0) values as a function of reaction catalyzed with the 5Co/ZSM-5-B catalyst (catalyst concentration: 1 wt%; methanol/oleic acid molar ratio: 30).

Figure 13 shows the C/C_0 values as a function of reaction time at 160 °C. In the blank reaction, the C/C_0 value was almost unchanged in the absence of catalysts. When the pure ZSM-5-A was used as the catalyst, the oleic acid conversion was lower than 8% after 180 min of reaction. When the Co/ZSM-5-A catalysts were used, the C/C_0 value significantly decreased as the reaction proceeded, indicating that the conversion of oleic acid was gradually increased. The catalytic activity of the Co/ZSM-5-A catalysts increased with an increase in Co content. Approximately 76% of oleic acid was converted with the 10Co/ZSM-5-A catalyst after 180 min of reaction.

For the Co/ZSM-5-B catalysts (Figure 14, the oleic acid conversion was greater than that achieved on the Co/ZSM-5-A catalysts. The best catalyst, 10 wt% Co/ZSM-5-B, could convert approximately 83.5% of the oleic acid within 180 min. The higher catalytic activity of the Co/ZSM-5-B catalysts than that of the Co/ZSM-5-A catalysts may be related to the greater amount of surface acidity and the higher dispersion and reducibility of Co_3O_4 on the Co/ZSM-5-B catalysts.

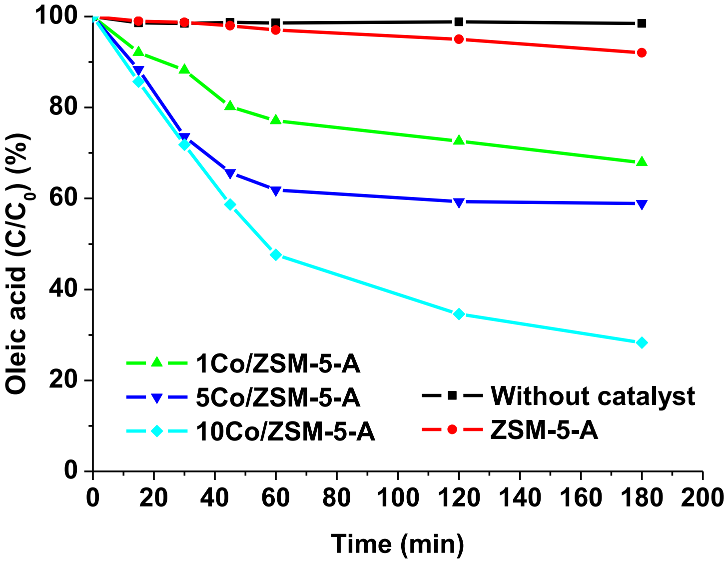

Figure 13. Oleic acid (C/C$_0$) values as a function of reaction catalyzed with Co/ZSM-5-A catalysts (catalyst mass: 1 wt%; temperature: 160 °C; methanol/oleic acid molar ratio: 30).

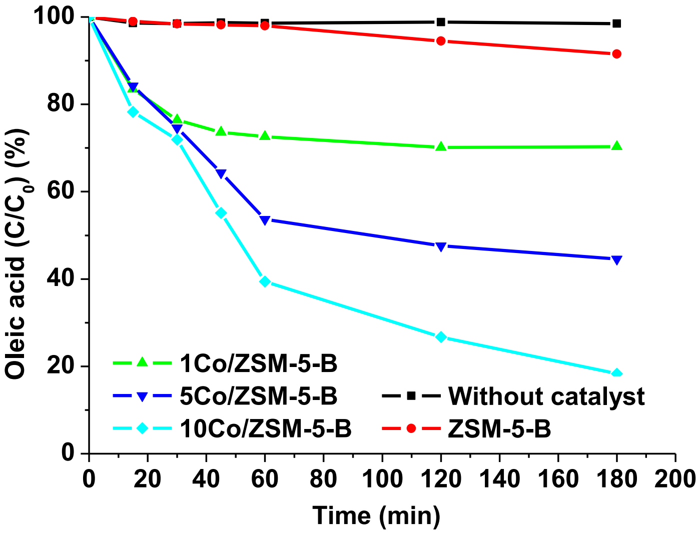

Figure 14. Oleic acid (C/C$_0$) values as a function of reaction catalyzed with Co/ZSM-5-B catalysts (catalyst concentration: 1 wt%; reaction temperature: 160 °C; methanol/oleic acid molar ratio: 30).

The effect of the catalyst concentration on the esterification reaction is shown in Figure 15. As the catalyst concentration was increased, the oleic acid conversion increased. For the 10Co/ZSM-5-A catalyst, as the catalyst concentration increased from 1 wt% to 2 wt%, the conversion increased from 76.0% to 95.1%. When 10Co/ZSM-5-B was used as catalyst, the oleic acid conversion increased from 82.5% to 95.8% as the catalyst concentration increased from 1 wt% to 2 wt%. As the catalyst amount further increased to 3 wt% and 4 wt%, the oleic acid conversion was not significant. Therefore, in the present experiment, the optimal catalyst concentration was 2 wt%.

The biodiesel selectivity achieved with different catalysts under the optimal condition (160 °C, 2 wt% catalysts mass, oleic acid oil to methanol molar ratio 30) is shown in Figure 16. For both series of catalysts, the highest biodiesel selectivity was obtained with the catalysts with 10 wt% Co, where they contained the most number of acid sites. ZSM-5 with surface acidity showed very low biodiesel selectivity, indicating that only surface acidity is insufficient for oleic acid esterification to ester. The selectivity increased with the Co content on the catalysts. On the most active catalyst, 10Co/ZSM-5-B, 82.5% of biodiesel selectivity was obtained. Therefore, the esterification of oleic acid with methanol on the Co/SZM-5 catalysts probably followed a bifunctional reaction mechanism involving surface acidity and metal function, which is discussed and proposed in the next part of this paper.

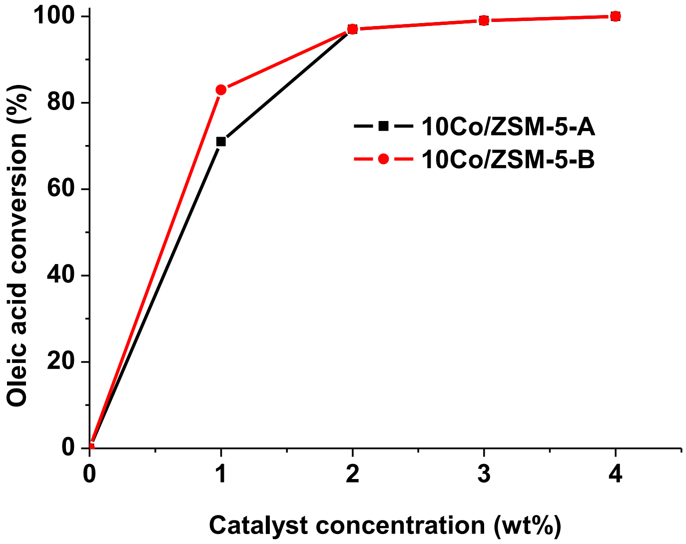

Figure 15. Oleic acid conversion vs catalysts concentration. Reaction condition: methanol/oleic acid molar ratio: 30; reaction temperature 160 °C; reaction time: 180 min.

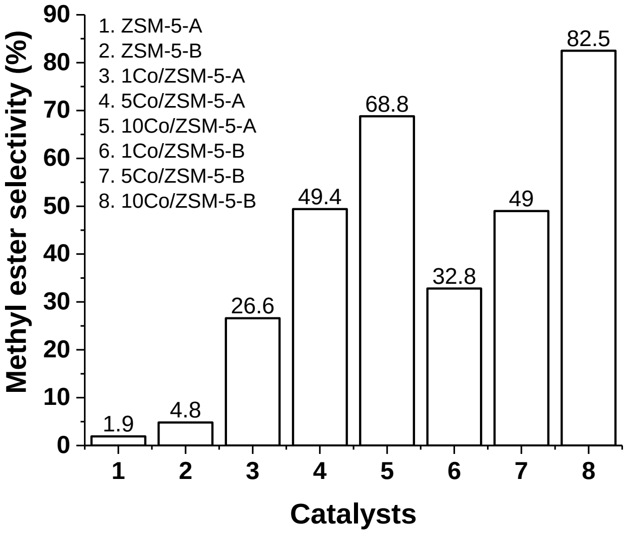

Figure 16. Biodiesel selectivity achieved on different catalysts (Reaction temperature: 160 °C; catalysts mass: 2 wt%; reaction time: 180 min; oleic acid oil to methanol molar ratio: 30).

The reusability of the most active catalyst, 10Co/ZSM-5-B, was evaluated five times under the optimal reaction conditions (methanol/oleic acid molar ratio of 30:1, catalyst concentration of 2 wt%, reaction temperature of 160 °C, and reaction time of 3 h). After each 3 h of reaction, the catalyst sample was filtered and washed. It was then calcined at 550 °C for 3 h in air before reuse for the catalytic evaluation. The recycled results are shown in Figure S3 in the Supplementary Materials.

For the fresh 10Co/ZSM-5-B catalyst, 95.1% oil conversion was obtained. However, the oleic acid conversion gradually decreased after the third reaction run. In the fifth recycling run, oleic acid conversion dropped to 84.7%. It was found that catalyst mass was partially lost during the filtration and washing operations. We believe that the catalyst activity deterioration principally resulted from the loss of catalyst mass during the operation procedure. However, after several reaction runs, the possibility of the active site blocking and acidity loss cannot be ruled out; they may also be the reasons for the catalyst deactivation. In the future, a catalyst deactivation investigation will be performed by focusing on the influence of textural properties and surface acidity changes.

The results obtained in the present work were compared with those obtained for other catalysts under similar reaction conditions (Table 3). Mohebbi et al. reported an oleic acid conversion 97% over a sulfated doped ZSM-5 catalyst [46]. However, their reaction was performed at a higher temperature (190 °C) with longer time (8 h) and higher catalyst concentration (5 wt%) than that used in the present work (160 °C, 3 h and catalyst concentration 2 wt%). In another work, in which a 20.5% WO_3/USY catalyst was applied for oleic acid esterification at a higher temperature (200 °C) and an expensive 20.5 wt% WO_3 was used as the dopant, the oleic acid conversion was only 77.9% [47], which was lower than the conversion of 95.1% that was obtained in the present work. When 3.5 wt% zeolite–Hβ was used as the catalyst, the oleic acid conversion was 82% [48]. Although the reaction temperature in this work was relatively low (60 °C), 10 h of the reaction time was required to reach 82% conversion. In another work reported by Gomes et al., in which 10 wt% of FAU zeolite Y was used as the catalyst, oleic acid conversion reached 92% at 100 °C with an oil-to-methanol ratio of 3:1 and a reaction time of 5 h [49]. Our results confirmed that the Co_3O_4 -doped ZSM-5 with a higher Si/Al ratio (Si/Al = 150) showed higher catalytic activity and could effectively convert oleic acid into biodiesel at a mild reaction condition.

Table 3. Comparison of the present work with the results obtained from other catalysts.

Catalysts	Feedstock	Alcohol to Oleic Acid Ratio	Reaction Condition	Conversion (%)	Ref.
SO_4^{2-}/ZSM-5	Oleic acid and methanol	20:1	Catal. concentration: 5 wt%; 190 °C, 8 h	97.0	[46]
20.5% WO_3/USY	Oleic acid and ethanol	6:1	Catal. concentration: 10 wt%, 200 °C, 2h.	77.9	[47]
Zeolite-Hβ	Oleic acid and methanol	20:1	Catal. concentration: 3.5 wt%, 60 °C, 10 h.	82.0	[48]
FAU zeolites-Y	Oleic acid and methanol	3:1	Catal. concentration: 10 wt%, 100 °C, 5 h.	92.0	[49]
Co_3O_4/ZSM-5-B	Oleic acid and methanol	30:1	Catal. concentration: 2 wt%, 160 °C, 3 h.	95.1	This work

2.8.2. Biodiesel Characterization by FTIR

Oleic acid and biodiesel were compared using the FTIR spectroscopic technique, as shown in Figure 17. The corresponding assignments of the various IR bands are reported in Table 4.

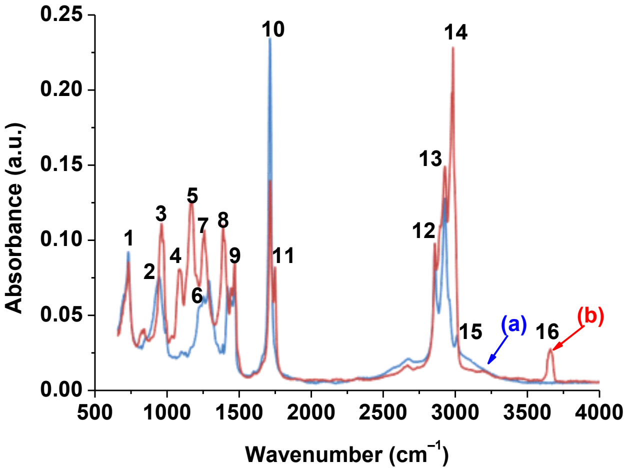

Figure 17. FTIR spectrum of oleic acid (**a**) and biodiesel (**b**) obtained using the 10Co/ZSM-5-A catalyst.

Table 4. Tentative peak assignment of the bands in FTIR spectra of oleic acid and biodiesel obtained using 10Co/ZSM-5-B.

Peak No.	Frequency (cm^{-1})	Band Assignments
1	725	CH_2 deformation, bending
2	920	C–OH stretching –OH bending
3	980	C–OH stretching
4	1100	C–OH stretching
5	1200	C–O stretching and C–O–C deformation
6 and 7	1250–1260	C–O stretching
8	1380	stretching –CH_3 of acyl chains (–$COOCH_3$)
9	1485	C–H deformation or bending in –CH_2 and –CH_3 groups
10	1720	C=O stretching in –COOH
11	1730	C=O stretching in –$COOCH_3$
12	2850	C–H symmetric stretching in –CH_2
13	2925	C–H asymmetric stretching in –CH_2
14	2955	C–H asymmetric stretching in –CH_3 in acyl chains
15	3010	C–H stretching in =C–H, C=C double bond
16	3600	–OH stretching in water

The IR bands in four regions (1000~1250 cm^{-1}, 1300~1500 cm^{-1}, 1700~1760 cm^{-1}, and 2900~3050 cm^{-1}) were observed. The IR signals at 1200 cm^{-1} and 1177 cm^{-1} were assigned to the vibration of the C–O bond corresponding to the methoxy group in the ester bonds [50,51]. The bands with moderate intensity, at approximately 1470 and 1485 cm^{-1}, were attributed to the C–C bond in the hydrocarbon chain and the extension vibration of the –CH_3 group. The strong band at 1735 cm^{-1} was assigned to the vibrations of the C=O in the carbonyl group of ester [52–56]. Usually, the IR bands of biodiesel between 2800 cm^{-1} and 3010 cm^{-1} correspond to the asymmetric and symmetrical stretching vibration modes of the C–H bond in the –CH, –CH_2, and –CH_3 in the hydrocarbon chains, respectively [53–59]. In Figure 17, three IR bands at 2925 cm^{-1}, 2850 cm^{-1}, and 725 cm^{-1} can be seen before and after the esterification reaction. They corresponded to the stretching vibration of –CH_2 in the acyl chain of fatty acids and biodiesel. The new IR band at 1380 cm^{-1} (No. 8), together with the new band at 2955 cm^{-1} (No. 14), were assigned to the stretching vibration of –CH_3 in acyl chains (–$C{=}OOCH_3$) [53]. These two new bands were very strong, indicating the formation of biodiesel.

It is noted that one band appeared at approximately 3600 cm^{-1} after the esterification reaction, which corresponds to the vibration of the –OH bond, indicating that water was produced during the esterification reaction.

In sum, the bands of No. 4, 5, 8, 11, and 14 in the FTIR spectrum provided clear evidence of the presence of the typical bands of carboxyl bond in the ester product, confirming the formation of biodiesel after the esterification reaction. Some IR bands overlapped with both oleic acid and biodiesel, resulting from the similarity of their hydrocarbon chains.

2.9. Discussion of the Bifunctional Mechanism

Based on the results obtained in this work, we postulated a mechanism of combining metal function with acidity function for the Co/ZSM-5 catalysts, which is chiefly responsible for the esterification of oleic acid. The proposed reaction mechanism consisted of four steps, as pictured in Scheme 1:

On the surface of the ZSM-5 support and the Co/ZSM-5 catalysts were both B acid sites and L acid sites. The number of the B and L acid sites increased with the increase in Co content. Because the acidity of the catalysts was correlated with the oleic acid conversion (Figures 9, 13 and 14), the surface acidities participated in the reaction as active centers, where the B acid sites served as proton acceptor/donator and the L acid sites served as electron acceptors. Therefore, in Scheme 1, Co_3O_4 nanoparticles, B acid sites, and L acid sites are noted as adsorption and surface reaction centers.

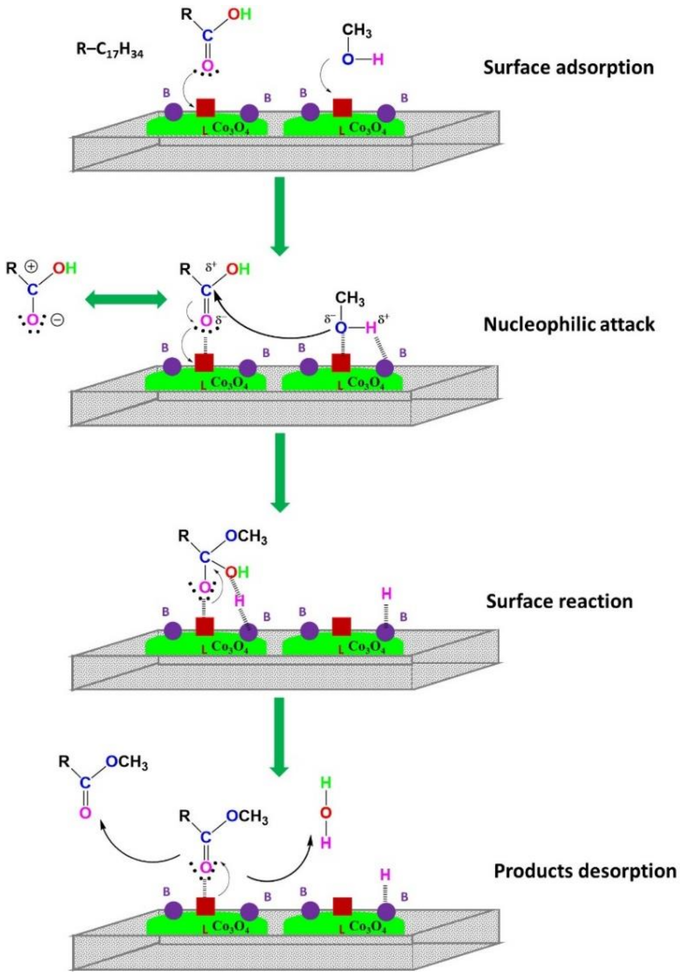

Scheme 1. Surface reaction mechanism of oleic acid esterification with ethanol. L: Lewis acid sites; B: Brønsted acid sites; R: –$C_{17}H_{34}$.

In the surface adsorption step, the —COOH head of oleic acid can preferentially adsorb on the L acid sites (Co^{3+} or Co^{2+}) via its electron pair in the O atom of the double bond interacting with the L acid sites. The electron shift from the O atom to the L acid sites in the catalyst forms the positively charged carbocation ($C_{17}H_{32}C^+OOH$) [52,60]. Because the reaction temperature was as high as 160 °C, methanol was at the evaporation state. The methanol molecule interacted with the B and L acid sites of the catalyst, thereby improving its polarity; the proton H^+ in the hydroxyl group of CH_3–O–H was transferred to the B acid sites, generating CH_3O^- species that associated with the L acid sites via donating its electron pair.

In the nucleophilic attack and surface reaction steps, the –COOH head of the adsorbed oleic acid in the L acid sites was attacked by the vicinaged CH_3O^- species. The nucleophilic attack of the negatively charged CH_3O^- in the L acid sites to the positively charged carbocation ($C_{17}H_{32}C^+OOH$) produced a ($C_{17}H_{32}COOCH_3OH$) intermediate; simultaneously, the H^+ proton in the B acid sites attacked the –OH of this intermediate, generating an unstable carbocation ($C_{17}H_{32}COOCH_3OH_2$). After releasing one H_2O molecule, the intermediate was transferred to the alkyl ester of the biodiesel ($C_{17}H_{32}COOCH_3$) [61,62]. Therefore, both the B and L acids sites participated in the esterification of oleic oil and played important roles in the electron transfer and intermediate formation.

It is noteworthy that the bare ZSM-5 zeolites showed rather low catalytic activity for the oleic acid esterification, although they had L and B acid sites. In the absence of metal oxide doping, it is impossible to achieve high oleic acid conversion over pure ZSM-5-A or ZSM-5-B. Therefore, the zeolite with surface acidity was not sufficient to catalyze the oleic acid esterification with high efficiency. After immobilizing Co_3O_4 on the ZSM-5 support, the oleic acid conversion was significantly enhanced by approximately 10 times compared with the oleic acid conversion that was achieved with the corresponding ZSM-15 zeolites. It is well known that the electron configuration of Co^{2+} and Co^{3+} are $[Ar]3d^7$ and $[Ar]3d^6$, respectively. Both Co^{2+} and Co^{3+} have unoccupied 3d electron orbitals, which can serve as electron acceptors. Therefore, the Co^{2+} and Co^{3+} in the dispersed Co_3O_4 accepted unshared electron pairs from the adsorbed reactants (herein, $C_{17}H_{32}COOH$ or CH_3OH), favoring the formation of $C_{17}H_{32}C^+OOH$ and CH_3O^- species. This undoubtedly promotes esterification efficiency. Therefore, the metal function (herein $Co_3O_{4)}$, also plays an important role in the esterification reaction of oleic acid. Both the metal oxide (Co_3O_4) and the surface acidity are responsible for the enhancement of oleic acid esterification.

The catalytic activity of the Co/ZSM-5-B catalysts was higher than that of Co/ZSM-5-A catalysts. This must be related to the difference in the amount of surface acidity and the reducibility of cobalt oxides. The Co/ZSM-5-B catalysts had acidity that was 10% to 15% greater than that of the Co/ZSM-5-A catalysts. In addition, the Co/ZSM-5-B catalysts showed better dispersion of Co_3O_4, as evidenced by the XRD analysis and TEM observation, and higher reducibility, as indicated by the TPR-H_2 characterization. The higher reducibility or the greater trapping electron ability of Co^{3+} and Co^{2+} in the Co_3O_4 of the Co_3O_4/ZSM-5-B rendered the adsorption of $C_{17}H_{32}COOH$ on the L acid sites (Co^{3+} or Co^{2+}) easier. As a result, the greater acid amount and the higher reducibility of Co_3O_4 in the Co/ZSM-5-B catalysts favored the enhancement of oleic acid esterification. Furthermore, we note that water was produced in the oleic acid esterification. Co/ZSM-5-B catalysts with a high Si/Al ratio (150) possessed high hydrophobicity, which may suppress water adsorption. This capacity allows easier access of hydrophilic reactants, such as methanol and oleic acid, to the active sites and products desorption, shifting the equilibrium esterification reaction forward and enhancing the oleic acid conversion.

With respect to the surface acid catalysis, the distribution and balance of the B and L acid sites on the surface of the catalysts are also important. We note that the pure ZSM-5-A presented many L acid sites together with some B acid sites. In contrast, ZSM-5-B had many B acid sites but a small number of L acid sites. The B/L ratio was approximately 0.31 for ZSM-5-A and 5.27 for ZSM-5-B. Clearly, both pure zeolites presented unbalanced B and L acid sites, which is probably one of the reasons that led to their catalytic activity being lower. Due to the fact that both B and L simultaneously took part in the esterification procedure, the unbalanced B and L acid sites did not benefit the surface reaction or the formation of the intermediate. The cobalt oxide immobilization on ZSM-5 created new acid sites and modified their distribution. The B/L ratio fell to the range of 0.61 to 0.80 for the Co/ZSM-5-A catalysts and 1.75 to 1.94 for the Co/ZSM-5-B catalysts, depending on the Co loading. Based on this work, a B/L value ranging from 0.8 to 1.9 will be beneficial to the oleic acid esterification.

In summary, the oleic acid esterification over the cobalt oxide-doped zeolite catalysts follows the bifunctional catalytic mechanism of combining the surface acidity and the metal function. Both the B and L acid sites participated in the surface adsorption and reaction, and a balanced B/L ratio was required to achieve high conversion and methyl ester selectivity. Cobalt oxide doping created more acid sites to obtain the B/L ratio in a range that favored oleic acid conversion. The greater reducibility of the dispersed Co_3O_4 nanoparticles and a balanced B/L molar ratio in the catalysts enhanced the catalyst activity.

3. Materials and Methods

3.1. Catalyst Preparation

The mesoporous ZSM-5 zeolites with molar ratios of SiO_2/Al_2O_3 50 and 150 were obtained from the Zeolyst International Company (Kansas City, KS, USA). The cobalt supported catalysts were prepared by using the incipient wetness impregnation method with an aqueous solution of $Co(NO_3)_2$ (Sigma-Aldrich, >99%, St. Louis, MO, USA) in order to obtain 1, 5, and 10 wt% of cobalt in the Co/ZSM-5 catalysts. All of the Co/ZSM-5 catalysts were calcined at 500 °C for 10 h under air atmosphere before the catalytic test. The catalysts were denoted as XCo/ZSM-5-A and XCo/ZSM-5-B, where X represented the weight percentage of Co and A and B represented the Si/Al molar ratio of 50 and 150 in zeolite, respectively.

3.2. Catalyst Characterization

3.2.1. N_2 Adsorption–Desorption Isotherms

The textural properties of the ZSM-5 support and the Co/ZSM-5 catalysts were measured on a Nova 4000 Series instrument (Quantahrome Instruments, Boynton Beach, FL, USA). An 0.3 g sample was degassed under vacuum at 100 °C for 24 h before N_2 adsorption. The surface areas were determined by nitrogen adsorption–desorption isotherms using the Brunauer–Emmett–Teller (BET) method. The average pore size distribution was determined by means of the Barret–Joyner–Halenda (BJH) method, using the data obtained from the desorption branch of the isotherm loops.

3.2.2. Atomic Absorption (AA) Spectroscopy

The Si/Al ratio and Co element content in the catalysts were analyzed using atomic absorption spectroscopy on a Spectronic-AA-20 spectrometer (Rochester, NY, USA) equipped with graphite tube atomizing (GTA). First, 100 mg of catalyst were dissolved in a 10 mL solution of aqua regia that consisted of three parts hydrochloric acid and one part nitric acid. This mixture was poured into a spiral plastic container that was sealed at a pressure of 5 psi. The thermal treatment of the sample was set in a microwave oven for 30 min in order to entirely dissolve the solid in the acid solution. The cobalt concentration in the sample was determined by the corresponding lamp pattern and the atomic absorption spectrophotometer curve.

3.2.3. X-ray Diffraction (XRD)

The X-ray diffraction patterns of the ZSM-5-A and ZSM-5-B supports and the Co/ZSM-5 catalysts were obtained using a SIEMENS D-500 diffractometer (Munich, Germany) with an anode of Cu and a monochromator of secondary beam. The identification of phase components was made in the two-theta range between 5° and 60°, using JCPDS reference cards No. 00-044-0002 and JCPDS Card No. 05-0727, corresponding to ZSM-5 zeolite and cobalt oxide, respectively.

3.2.4. Raman Spectroscopy

Raman spectra of the Co dispersed catalysts were obtained in air at room temperature using 633 nm radiations from a Ne ion laser equipped with a CCD detector. The spot size of 1 μm diameter and potency varying from 70 μW to 175 μW were employed. The Raman spectra were recorded on a Labram HR800 Raman spectrometer (LabRAM HR800 model, HORIBA, Paris, France) within the wavenumber range from 100 cm^{-1} to 1200 cm^{-1}.

3.2.5. In Situ FTIR of Pyridine Adsorption

The amount and strength of acidity on the supports and the Co/ZSM-5 catalysts were determined by an in situ pyridine adsorption of infrared spectroscopy (FTIR) study using a Fourier Transformation Nicolet 170 SX instrument. The solid material powders were pressed into a thin self-supported wafer. Then, it was placed in a glass Pyrex cell with CF2 windows coupled to a vacuum line, in order to be evacuated (1×10^{-6} Pa) in situ at 400 °C for 30 min. The pyridine adsorption was carried out in the IR cell at 25 °C. Then, the adsorbed pyridine was desorbed under vacuum as the temperature increased from room temperature to 400 °C. The quantities of the adsorbed pyridine were obtained from the integrated absorbance bands. The total number of pyridine adsorbed on the surface (μmoles/g) was obtained by applying the Beer–Lambert law through the following equation:

$$\text{N (pyridine) adsorbed} = \text{Ai} \times \text{S/W} \times \varepsilon \tag{3}$$

where Ai is the absorbance maximum of the absorption bands obtained from the IR spectra; S is the area of the sample wafer used in the experiment IR; W indicates the weight of the tablet; and ε is the molar extinction coefficient of pyridine adsorbed on zeolite (ε = 0.9374 cm/mol).

3.2.6. H_2-Temperature Programmed Reduction (H_2-TPR)

The H_2-TPR experiments were performed with CHEMBET-3000 (QuantaChrome Instrument, Boynton Beach, FL, USA) equipment by means of the following protocol: 0.2 g samples were heated at 300 °C under nitrogen flow (10 mL·min^{-1}) for 30 min. Then, the samples were cooled to room temperature. A mixture of gas flow (5% H_2 + 95% N_2) was then passed through the glass cell. The TPR profiles were registered using a heating program of 10 °C/min from ambient temperature to 700 °C at a flow rate of 10 mL/min.

3.2.7. Transmission Electron Microscopy (TEM)

The TEM observations were performed using a JEM-ARM200CF microscope (JEOL, Tokyo, Japan) at 200 kV under operating conditions of 10^{-4} mbar vacuum, with resolution 1.7 Å and point amplification 1.25×10^5 to 3.15×10^6. To determine the average particle size of each catalyst, the following equation was used: $d_s = \Sigma n_i d_i^3 / \Sigma n_i d_i^2$, where d_s is the average particle size; di is the particle diameter; and n_i is the number of particle diameter d_i.

3.3. Catalytic Activity Tests

Oleic acid (Interlab, Madrid, Spain, 99.8%), methanol (J.T. Baker, Toluca, Mexico, 99.90%) and the Co/ZSM-5 catalysts were placed in a 300 mL Parr reactor under constant mechanical stirring (650 rpm). The esterification reactions of oleic acid were carried out at 140 °C to 160 °C with a molar ratio of oleic acid/methanol of 1:30 and a catalyst concentration of 1 wt% to 4 wt% with respect to the mass of oleic acid. The reaction was maintained for 3 h under self-generated pressure (approximately 30 bars). The reaction procedure was monitored by taking samples at 5, 10, 20, 30, 60, 120, and 180 min and the aliquots were analyzed by a gas chromatography analyzer (VARIAN STAR 3400 CX) equipped with a capillary column DB-23 (length 30 m, internal diameter 0.53 mm, film thickness 1.0 μm). The carrier gas (He, 99.99%) was introduced at a rate 120 mL/min; the temperature of the FID detector was controlled at 250 °C. The oleic acid conversion denoted as X was calculated with the following equation:

$$X\ (\%) = (1 - C/C_0) \times 100 \tag{4}$$

where C is the value of oleic acid amount at a time t and C_0 is the initial amount of oleic acid at $t = 0$. Biodiesel yield was calculated with the following equation:

$$\text{Biodiesel yield (\%)} = \text{mole of alkyl ester/mole of oleic acid in feed} \times 100 \tag{5}$$

The experimental data reported herein were an average of three measurements. The standard deviation varied within ±2.5%.

4. Conclusions

Two sets of Co/ZSM-5 nanocatalysts with mesoporous ZSM-5 zeolites as support were prepared. The Si/Al atomic ratio in the ZSM-5 affected the surface acidity and the cobalt oxide reducibility. The Co_3O_4 phase was formed on the zeolite surface after calcination at 500 °C, which could be reduced in two steps by hydrogen. Greater reducibility of Co_3O_4 was achieved on the Co/ZSM-5-B catalysts than on the Co/ZSM-5-A catalysts. All of the Co/SZM-5 catalysts contained both B and L acid sites, with a B/L ratio ranging from 0.61 to 1.94, depending on the Co loading. The surface acidity of the Co/ZSM-5 catalysts increased when the Co content was increased.

In the production of biodiesel using unsaturated omega-9 oleic acid as feedstock, the Co/ZSM-5-B catalysts showed higher catalytic activity. Under the optimal reaction conditions (temperature 160 °C, catalyst concentration 2 g/L, methanol/oleic acid molar ratio 30, and reaction time 180 min), a 95.1% oleic acid conversion with 83.5% selectivity to methyl ester was achieved on the best catalyst, 10 wt% Co/ZSM-5-B. The esterification activity of the catalysts was correlated with surface acidity, the balanced B/L ratio, and the reducibility of the Co_3O_4 nanoparticles. A larger number of B and L acid sites of the catalysts and the greater reducibility of Co_3O_4 nanoparticles favored the enhancement of catalytic activity and methyl ester selectivity. We found that the B/L ratio in the range of 0.8 to 1.9 benefited the esterification reaction. A bifunctional mechanism of the metal function combined with the acidity function of the Co/ZSM-5 catalysts was proposed.

Supplementary Materials: The following supporting information can be downloaded at: https://www.mdpi.com/article/10.3390/catal12080900/s1. The loops of N_2 adsorption-desorption isotherms of ZSM-5-A and ZSM-5-B and the reusability of 10Co/ZSM-5-B catalyst.

Author Contributions: Conceptualization, J.A.W.; methodology; J.A.W. and U.A.; investigation, F.N., U.A. and F.T.; data curation, S.O.F.; writing: F.N. and J.A.W.; writing—review and editing, L.C., L.E.N. and J.S.; supervision, J.A.W. and S.O.F.; funding acquisition, J.A.W., L.C. and L.E.N. All authors have read and agreed to the published version of the manuscript.

Funding: This research was funded by Instituto Politécnico Nacional grant number No. SIP-20210888, SIP-20210451. And The APC was funded by the Universidad Autónoma Metropolitana-Azcapotzalco.

Data Availability Statement: The data used in this work are available from the corresponding author, upon request.

Acknowledgments: F. Núñez is also grateful for the financial support of CONACyT–Mexico for his postdoctoral investigation.

Conflicts of Interest: The authors declare no conflict of interest.

References

1. Melero, J.A.; Bautista, L.F.; Iglesias, J.; Morales, G.; Sanchez, R. Production of biodiesel from waste cooking oil in a continuous packed bed reactor with an agglomerated Zr-SBA-15/bentonite catalyst. *Appl. Catal. B Environ.* **2014**, *145*, 197–204. [CrossRef]
2. Lam, M.K.; Lee, K.T.; Mohamed, A.R. Homogeneous, heterogeneous and enzymatic catalysis for transesterification of high free fatty acid oil (waste cooking oil) to biodiesel: A review. *Biotech. Adv.* **2010**, *28*, 500–518. [CrossRef] [PubMed]
3. Choi, K.-M.; Harshavardhan, S.J.; Sridhar, C.; Kumar, D.; Jang, K. Synthesis of POSS derived organic-inorganic hybrid esters for insulating oil applications. *Bull. Korean Chem. Soc.* **2014**, *35*, 2769–2773. [CrossRef]
4. Chew, T.L.; Bhatia, S. Catalytic processes towards the production of biofuels in a palm oil and oil palm biomass-based biorefinery. *Bioresour. Technol.* **2008**, *99*, 7911–7922. [CrossRef] [PubMed]
5. Hsiao, M.C.; Lin, W.T.; Chiu, W.C.; Hou, S.S. Two-Stage Biodiesel Synthesis from Used Cooking Oil with a High Acid Value via an Ultrasound-Assisted Method. *Energies* **2021**, *14*, 3703. [CrossRef]
6. Ma, X.; Liu, F.; Helian, Y.; Li, C.; Wu, Z.; Li, H.; Chu, H.; Wang, Y.; Wang, Y.; Lu, W.; et al. Current application of MOFs based heterogeneous catalysts in catalyzing transesterification/esterification for biodiesel production: A review. *Energy Convers. Manag.* **2021**, *229*, 113760. [CrossRef]
7. Zakaria, Z.Y.; Linnekoski, J.; Amin, N.A.S. Catalyst screening for conversion of glycerol to light olefins. *Chem. Eng. J.* **2012**, *207–208*, 803–813. [CrossRef]
8. Leung, D.Y.C.; Wu, X.; Leung, M.K.H. A review on biodiesel production using catalyzed transesterification. *Appl. Energy* **2010**, *87*, 1083–1095. [CrossRef]
9. Kawashima, A.; Matsubara, K.; Honda, K. Acceleration of catalytic activity of calcium oxide for biodiesel production. *Bioresour. Technol.* **2009**, *100*, 696–700. [CrossRef]
10. Kouzu, M.; Tsunomori, M.; Yamanaka, S.; Hidaka, J. Solid base catalysis of calcium oxide for a reaction to convert vegetable oil into biodiesel. *Adv. Powder Technol.* **2010**, *21*, 488–494. [CrossRef]
11. Suryaputra, W.; Winata, I.; Indraswati, N.; Ismadji, S. Waste capiz (*Amusium cristatum*) shell as a new heterogeneous catalyst for biodiesel production. *Renew. Energy* **2013**, *50*, 795–799. [CrossRef]
12. Prabu, M.; Manikandan, M.; Kandasamy, P.; Kalaivani, P.; Rajendiran, N.; Raja, T. Synthesis of biodiesel using the Mg/Al/Zn hydrotalcite/SBA-15 nanocomposite catalyst. *ACS Omega* **2019**, *4*, 3500–3507. [CrossRef]
13. Shibasaki, N.; Honda, H.; Kuribayashi, H.; Toda, T.; Fukumura, T.; Yonemoto, T. Biodiesel production using ionic ion exchange resin as heterogeneous catalyst. *Bioresour. Technol.* **2007**, *98*, 416–421. [CrossRef] [PubMed]
14. Kulkarni, M.G.; Dalai, A.K. Waste cooking oil-an economical source for biodiesel: A review. *Ind. Eng. Chem. Res.* **2006**, *45*, 2901–2913. [CrossRef]

15. Snåre, M.; Mäki, P.; Simakova, I.L.; Myllyoja, J.; Murzin, D.Y. Overview of catalytic methods for production of next generation biodiesel from natural oils and fats. *Russian J. Phys. Chem. B* **2009**, *3*, 1035–1043. [CrossRef]
16. Lestari, S.; Simakova, I.; Tokarev, A.; Mäki, P.; Eränen, K.; Murzin, D.Y. Synthesis of biodiesel via deoxygenation of stearic acid over supported Pd/C catalyst. *Catal. Letts.* **2008**, *122*, 247–251. [CrossRef]
17. Mäki, P.; Snåre, M.; Eränen, K.; Myllyoja, J.; Murzin, D.Y. Continuous decarboxylation of lauric acid over Pd/C catalyst. *Fuel* **2008**, *87*, 3543–3549. [CrossRef]
18. Simakova, I.L.; Simakova, O.A.; Romanenko, A.V.; Murzin, D.Y. Hydrogenation of vegetable oils over Pd on nanocomposite carbon catalysts. *Ind. Eng. Chem. Res.* **2008**, *47*, 7219–7225. [CrossRef]
19. Fu, J.; Lu, X.; Savage, P.E. Hydrothermal decarboxylation and hydrogenation of fatty acids over Pt/C. *ChemSusChem* **2011**, *4*, 481–486. [CrossRef]
20. Madsen, A.T.; Ahmed, E.H.; Christensen, C.H.; Fehrmann, R.; Riisager, A. Hydrodeoxygenation of waste fat for diesel production: Study on model feed with Pt/alumina catalyst. *Fuel* **2011**, *90*, 3433–3438. [CrossRef]
21. Han, J.; Sun, H.; Ding, Y.; Lou, H.; Zheng, X. Palladium-catalyzed decarboxylation of higher aliphatic esters: Towards a new protocol to the second-generation biodiesel production. *Green Chem.* **2010**, *12*, 463–467. [CrossRef]
22. Han, J.; Sun, H.; Duan, J.; Ding, Y.; Lou, H.; Zheng, X. Palladium-Catalyzed Transformation of Renewable Oils into Diesel Components. *Adv. Synth. Catal.* **2010**, *352*, 1805–1809. [CrossRef]
23. Lestari, S.; Mäki, P.; Eränen, K.; Beltramini, J.; Max, G.Q.; Murzin, D.Y. Diesel-like hydrocarbons from catalytic deoxygenation of stearic acid over supported Pd nanoparticles on SBA-15 catalysts. *Catal. Letts.* **2009**, *134*, 250–257. [CrossRef]
24. Huber, G.W.; Corma, A. Synergies between Bio- and Oil Refineries for the Production of Fuels from Biomass. *Angew. Chem. Int. Ed.* **2007**, *46*, 7184–7201. [CrossRef] [PubMed]
25. Huber, G.W.; Iborra, S.; Corma, A. Synthesis of transportation fuels from biomass: Chemistry, catalysts, and engineering. *Chem. Rev.* **2006**, *106*, 4044–4098. [CrossRef]
26. Huber, G.W.; O'Connor, P.; Corma, A. Processing biomass in conventional oil refineries: Production of high quality diesel by hydrotreating vegetable oils in heavy vacuum oil mixtures. *Appl. Catal. A* **2007**, *329*, 120–129. [CrossRef]
27. Ma, F.; Hanna, M.A. Biodiesel production: A review. *Bioresour. Technol.* **1999**, *70*, 1–15. [CrossRef]
28. Gao, L.J.; Shang, Q.Q.; Zhou, J.J.; Xiao, G.M.; Wei, R.P. Esterification of Oleic Acid in Biodiesel Synthesis with SO_4^{2-}/ZrO_2/MCM-41 as Catalyst. *Asian J. Chem.* **2013**, *25*, 6579–6583. [CrossRef]
29. Narasimharao, K.; Brown, D.R.; Lee, A.F.; Newman, A.D.; Siril, P.F.; Tavener, S.J.; Wilson, K. Structure–activity relations in Cs-doped heteropolyacid catalysts for biodiesel production. *J. Catal.* **2007**, *248*, 226–234. [CrossRef]
30. Karinen, R.S.; Krause, A.O.I. New biocomponents from glycerol. *Appl. Catal. A Gen.* **2006**, *306*, 128–133. [CrossRef]
31. Wang, C.; Liu, Q.; Song, J.; Li, W.; Li, P.; Xu, R.; Ma, H.; Tian, Z. High quality diesel-range alkanes production via a single-step hydrotreatment of vegetable oil over Ni/zeolite catalyst. *Catal. Today* **2014**, *234*, 153–160. [CrossRef]
32. Silva, V.J.; Rodrigues, J.J.; Soares, R.R.; Napolitano, M.N.; Rodrigues, M.G. Cobalt supported on ZSM-5 zeolite using kaolin as silicon and aluminun sources for fischer-tropsch synthesis. *Braz. J. Petrol. Gas* **2013**, *7*, 083–094. [CrossRef]
33. Sing, K.S.W.; Evertt, D.H.; Haul, R.A.W.; Moscou, L.; Pierotti, R.A.; Rouquerol, J.; Siemieniewska, T. Reporting physisorption data for gas/solids systems with special reference to the determination of surface area and porosity. *Pure Appl. Chem.* **1985**, *57*, 603–619. [CrossRef]
34. Cheng, J.P.; Chen, X.; Wu, J.S.; Liu, F.; Zhang, X.B.; Dravid, V.P. Porous cobalt oxides with tunable hierarchical morphologies for supercapacitor electrodes. *Cryst. Eng. Comm.* **2012**, *14*, 6702–6709. [CrossRef]
35. Zhao, X.Q.; Veintemillas, S.; Bomati, M.O.; Morales, M.P.; Xu, H.B. Thermal history dependence of the crystal structure of Co fine particles. *Phys. Rev. B* **2005**, *71*, 024106. [CrossRef]
36. Li, Y.; Qiu, W.; Qin, F.; Fang, H.; Hadjiev, V.G.; Litvinov, D.; Bao, J. Identification of cobalt oxides with Raman Scattering and Fourier Transform Infrared Spectroscopy. *J. Phys. Chem. C* **2016**, *120*, 4511–4516. [CrossRef]
37. Baerlocher, C.; McCusker, L.B.; Olson, D.H. *Atlas of Zeolite Framework Types*, 6th ed.; Elsevier: Amsterdam, The Netherlands, 2007. Available online: http://www.iza-structure.org/books/Atlas_6ed.pdf (accessed on 20 May 2022).
38. Rivas, B.; Salgueiriño, V. Thermodynamic CoO–Co_3O_4 crossover using Raman spectroscopy in magnetic octahedronshaped nanocrystals. *J Raman Spectrosc.* **2017**, *48*, 837–841. [CrossRef]
39. Jongsomjit, B.; Goodwin, J. Co-support compound formation in Co/Al_2O_3 catalysts: Effect of reduction gas containing CO. *Catal. Today* **2002**, *77*, 91–204. [CrossRef]
40. Emeis, C.A. Determination of integrated molar extinction coefficients for infrared absorption bands of pyridine adsorbed on solid acid Catalysts. *J. Catal.* **1993**, *141*, 347–354. [CrossRef]
41. Morterra, C.; Magnacca, G. Surface characterization of modified aluminas. Part 4. Surface hydration and Lewis acidity of CeO_2–Al_2O_3 systems. *J. Chem. Soc. Faraday Trans.* **1996**, *92*, 1991–1999. [CrossRef]
42. González, J.; Wang, J.A.; Chen, L.F.; Manríquez, M.E.; Dominguez, J.M. Structural Defects, Lewis Acidity and Catalysis Properties of Mesostructured WO_3/SBA-15 Nanocatalysts. *J. Phys. Chem. C* **2017**, *121*, 23988–23999. [CrossRef]
43. Lohse, U.; Löfer, E.; Hunger, M.; Stöckner, J.; Patzelova, V. Hydroxyl groups of the non-framework aluminium species in dealuminated Y zeolites. *Zeolites* **1987**, *7*, 11–13. [CrossRef]
44. Chromčáková, Ž.; Obalová, L.; Kovanda, F.; Legut, D.; Titov, A.; Ritz, M.; Fridrichová, D.; Michalik, S.; Kuśtrowski, P.; Jirátová, K. Effect of precursor synthesis on catalytic activity of Co_3O_4 in N_2O decomposition. *Catal. Today* **2015**, *257*, 18–25. [CrossRef]

45. Boix, A.; Miro, E.; Lombardo, E.; Bañanes, M.; Mariscal, R.; Fierro, J. The nature of cobalt species in Co and PtCoZSM-5 used for the SCR of NOx with CH_4. *J. Catal.* **2003**, *217*, 186–194. [CrossRef]
46. Mohebbi, S.; Rostamizadeh, M.; Kahforoushan, D. Efficient sulfated high silica ZSM-5 nanocatalyst for esterification of oleic acid with metanol. *Microporous Mesoporous Mater.* **2020**, *294*, 109845. [CrossRef]
47. Costa, A.A.; Braga, P.R.S.; de Macedo, J.L.; Dias, J.A.; Dias, S.C.L. Structural effects of WO_3 incorporation on USY zeolite and application to free fatty acids esterification. *Microporous Mesoporous Mater.* **2012**, *147*, 142–148. [CrossRef]
48. Narkhede, N.; Patel, A. Efficient synthesis of biodiesel over a recyclable catalyst comprising a monolacunary silicotungstate and zeolite H-beta. *RSC Adv.* **2014**, *4*, 64379–64387. [CrossRef]
49. Gomes, G.J.; Dal Pozzo, D.M.; Zalazar, M.F.; Costa, M.B.; Arroyo, P.A.; Bittencourt, P.R.S. Oleic Acid Esterification Catalyzed by Zeolite Y-Model of the Biomass Conversion. *Top. Catal.* **2019**, *62*, 874–883. [CrossRef]
50. Xu, L.; Zhu, X.; Chen, X.; Sun, D.; Yu, X. Direct FTIR analysis of free fatty acids in edible oils using disposable polyethylene film. *Food Anal. Methods* **2015**, *8*, 857–863. [CrossRef]
51. Rabelo, S.N.; Ferraz, V.P.; Oliveira, L.S.; Franca, A.S. FTIR Analysis for quantification of fatty acid methyl esters in biodiesel produced by microwave-assisted transesterification. *Int. J. Environ. Sci. Dev.* **2015**, *6*, 964–969. [CrossRef]
52. Muik, B.; Lendl, B.; Molina, A.; Pérez, L.; Ayora, M.J. Determination of oil and water content in olive pomace using near infrared and Raman spectrometry. A comparative study. *Anal. Bioanal. Chem.* **2004**, *379*, 35–41. [CrossRef] [PubMed]
53. Shapaval, V.; Brandenburg, J.; Blomqvist, J.; Tafintseva, V.; Passoth, V.; Sandgren, M.; Kohler, A. Biochemical profiling, prediction of total lipid content and fatty acid profile in oleaginous yeasts by FTIR spectroscopy. *Biotechnol. Biofuels* **2019**, *12*, 140. [CrossRef] [PubMed]
54. Patel, A.; Narkhede, N. Biodiesel synthesis via esterification and transesterification over a new heterogeneous catalyst comprising lacunary silicotungstate and MCM-41. *Catal. Sci. Technol.* **2013**, *3*, 3317–3325. [CrossRef]
55. Pimentel, M.F.; Ribeiro, G.M.; Da Cruz, R.S.; Stragevitch, L.; Pacheco, J.; Teixeira, L. Determination of biodiesel content when blended with mineral diesel fuel using infrared spectroscopy and multivariate calibration. *Microchem. J.* **2006**, *82*, 201–206. [CrossRef]
56. De Lira, L.; De Vasconcelos, F.; Pereira, C.F.; Silveira, A.; Stragevitch, L.; Pimentel, M. Prediction of properties of diesel/biodiesel blends by infrared spectroscopy and multivariate calibration. *Fuel* **2010**, *89*, 405–409. [CrossRef]
57. Coronado, M.A.; Montero, G.; García, C.; Valdez, B.; Ayala, R.; Pérez, A. Quality Assessment of Biodiesel Blends Proposed by the New Mexican Policy Framework. *Energies* **2017**, *10*, 631. [CrossRef]
58. Samanta, S.; Sahoo, R.R. Waste Cooking (Palm) Oil as an Economical Source of Biodiesel Production for Alternative Green Fuel and Efficient Lubricant. *Bioenerg. Res.* **2021**, *14*, 163–174. [CrossRef]
59. Cruz, M.; Almeida, M.F.; Alvim, M.D.C.; Dias, J.M. Monitoring Enzymatic Hydroesterification of Low-Cost Feedstocks by Fourier Transform InfraRed Spectroscopy. *Catalysts* **2019**, *9*, 535. [CrossRef]
60. Hanif, M.A.; Nisar, S.; Rashid, U. Supported solid and heteropoly acid catalysts for production of biodiesel. *Catal. Rev.* **2017**, *59*, 165–188. [CrossRef]
61. Brahmkhatri, V.; Patel, A. 12-Tungstophosphoric acid anchored to SBA-15: An efficient, environmentally benign reusable catalysts for biodiesel production by esterification of free fatty acids. *Appl. Catal. A* **2011**, *403*, 161–172. [CrossRef]
62. Endalew, A.K.; Kiros, Y.; Zanzi, R. Inorganic heterogeneous catalysts for biodiesel production from vegetable oils. *Biomass Bioenerg.* **2011**, *35*, 3787–3809. [CrossRef]